Dalton Transactions

PAPER

View Article Online
View Journal | View Issue

Cite this: *Dalton Trans.*, 2015, **44**, 9496

Two novel POM-based inorganic–organic hybrid compounds: synthesis, structures, magnetic properties, photodegradation and selective absorption of organic dyes†

Xue-Jing Dui,[a,b] Wen-Bin Yang,*[a,c] Xiao-Yuan Wu,[a,c] Xiaofei Kuang,[a,c] Jian-Zhen Liao,[a,b] Rongmin Yu[a,c] and Can-Zhong Lu*[a,c]

Received 16th March 2015,
Accepted 16th April 2015

DOI: 10.1039/c5dt01042j

www.rsc.org/dalton

The hydrothermal reactions of a mixture of $(NH_4)_6Mo_7O_{24}{\cdot}4H_2O$, $Cu(Ac)_2{\cdot}H_2O$ and 3-bpo ligands at different temperatures result in the isolation of two novel inorganic–organic hybrid materials containing different but related isopolymolybdate units, $[Cu(3\text{-bpo})(H_2O)(Mo_4O_{13})]{\cdot}3H_2O$ (**1**) and $[Cu_2(3\text{-bpo})_2(Mo_6O_{20})]$ (**2**). The $\{Mo_4O_{13}\}_n$ chains in **1** and unprecedented $[Mo_6O_{20}]^{4-}$ isopolyhexamolybdate anions in **2** are linked by octahedral Cu^{2+} ions into two-dimensional hybrid layers. Interestingly, 3-bpo ligands in both **1** and **2** are located on either side of these hybrid layers and serve as arched footbridges to link Cu(II) ions in the layer *via* pyridyl N-donors, and at the same time connect these hybrid layers into 3D supramolecular frameworks *via* weak $Mo{\cdots}N_{oxadiazole}$ bonds. Another important point for **1** is that water clusters are filled in the 1D channels surrounded by isopolytetramolybdate units. In addition, dye adsorption and photocatalytic properties of **1** and magnetic properties of **1–2** have been investigated. The results indicated that complex **1** is not only a good heterogeneous photocatalyst in the degradation of methyl orange (MO) and methylene blue (MB), but also has high absorption capacity of MB at room temperature and can selectively capture MB molecules from binary mixtures of MB/MO or MB/RhB. All MB molecules absorbed on **1** can be completely released and photodegraded in the presence of adequate peroxide. The temperature dependence of magnetic susceptibility revealed that complex **2** exhibits antiferromagnetic ordering at about 5 K, and a spin-flop transition was observed at about 5.8 T at 2 K, indicating metamagnetic-like behaviour from antiferromagnetic to ferromagnetic phases.

Introduction

Polyoxometalates (POMs) are a kind of inorganic metal-oxide clusters that are assembled by early transition metal MO_x polyhedra *via* sharing corners, edges and/or faces, and have abundant topologies and compositions, acid/base tunability and diverse electronic and photochemical properties. So far, a huge number of polyoxometalates have been synthesized and applied widely in fields of catalysis, medicine, electronics, magnetism and optics.[1–5] Recently, a new arising research topic in this field is the use of POMs as inorganic building blocks to construct inorganic–organic hybrid materials with various metal–organic coordination fragments. From the structural point of view, the polyoxometalate anions in these hybrids, can be either connected as guests/templates/counter ions through noncovalent interactions,[1a,b] or coordinated to metal atoms as inorganic ligands by covalent bonds.[1e,f] Therefore, the POM-supported hybrid materials combine the advantages of inorganic polyoxometalates and the functionalities of organic components, which make them attractive for many new potential applications ranging from gas storage, chemical separation and catalysis to ion exchange reactions.

Besides Keggin heteropolyoxometalates in the big family of POMs, $[Mo_8O_{26}]^{4-}$ octamolybdates are also very easily prepared or *in situ* formed from reaction precursors under hydrothermal conditions and controlled pH values. Furthermore, according to the different numbers and arrangement of MoO_4, MoO_5, and MoO_6 polyhedra, at least nine types of octamolybdate isomers (*i.e.* α-, β-, γ-, δ-, ε-, ζ-, η-, θ- and ι-$[Mo_8O_{26}]^{4-}$) have

[a]*Key Laboratory of Design and Assembly of Functional Nanostructures, Fujian Institute of Research on the Structure of Matter, Chinese Academy of Sciences, China. E-mail: czlu@fjirsm.ac.cn, ywb@fjirsm.ac.cn; Fax: +86-591-83714946; Tel: +86-591-83705794*

[b]*University of Chinese Academy of Sciences, Beijing, 100049, China*

[c]*Fujian Provincial Key Laboratory of Nanomaterials, Fujian Institute of Research on the Structure of Matter, Chinese Academy of Sciences, China*

†Electronic supplementary information (ESI) available: Additional figures, powder XRD patterns, TG curves, and optical absorption spectra. CCDC 1003521 for **1** and 1003522 for **2**. For ESI and crystallographic data in CIF or other electronic format see DOI: 10.1039/c5dt01042j

been reported so far.[6–8] These octamolybdate isomers exhibit rather good coordination abilities with various metal ions and show certain self-assembly abilities to form infinite inorganic chains.[9] As a result, octamolybdates and their derivative species have been used widely as important inorganic building units to construct host–guest structures[10] and inorganic–organic hybrid materials.[8,11] To date, remarkable hybrid materials based on isolated iso- or heteropolyoxometalates have been reported, however, examples of inorganic–organic hybrid materials based on 1D chains or 2D layers of polyoxometalates are still very rare,[12] indicating a research area still in its infancy, and an arduous challenge for POM chemists to rationally design and synthesize POM-supported inorganic–organic hybrid materials.

Another important point in the synthesis of novel POM-supported inorganic–organic hybrid materials is to choose a suitable organic ligand, because the length, geometry and coordination ability of the organic ligands play important roles in generating frameworks. For example, the polydentate N-containing ligands, such as 2,2′-bipy, 1,10-phen, 4,4′-bipy and 2,4,6-tris(4-pyridyl)-1,3,5-triazine, have been employed extensively as chelating or bridging linkers due to their diversity of the connecting modes and the high structural stability. Herein, we choose the ligand 2,5-bis(3-pyridyl)-1,3,4-oxadiazole (3-bpo) to build POM-supported inorganic–organic hybrid materials, because it exhibits diverse coordination/bridging modes as reported recently in metal–organic coordination polymers,[13] exhibits a certain degree of flexibility presented by the changeable angles between two pyridyl rings and central oxadiazole ring, and can be *in situ* converted into a more stable 3,5-bis(3-pyridyl)-1,2,4-triazolate ligand under suitable solvothermal conditions.[14] As expected, the hydrothermal reactions of $(NH_4)_6Mo_7O_{24}{\cdot}4H_2O$ and $Cu(Ac)_2{\cdot}H_2O$ with 3-bpo under different temperatures and pH values afforded two novel POM-based inorganic–organic hybrids, namely, $[Cu(3\text{-bpo})(H_2O)(Mo_4O_{13})]{\cdot}3H_2O$ (**1**) and $[Cu_2(3\text{-bpo})_2(Mo_6O_{20})]$ (**2**). Interestingly, the isopolytetramolybdate unit in complex **1**, consisting of four MoO_5 square pyramids with common edges, can be viewed as the half of centro-symmetric β-$[Mo_8O_{26}]^{4-}$, and are extended into infinite chains $\{Mo_4O_{13}\}_n$ through sharing corners, while the isopolyhexamolybdate unit $[Mo_6O_{20}]^{4-}$ in **2** represents an unprecedented type of hexamolybdates completely different from Anderson and Lindquist $[Mo_6O_{19}]^{2-}$ hexamolybdates, and other hexamolybdates.[15,16] The $\{Mo_4O_{13}\}_n$ chains in **1** and isopolyhexamolybdate units in **2** are joined together by Cu(II) ions into 2D layers further connected into 3D supramolecular frameworks *via* weak Mo···N bonds (*ca.* 2.65 Å). In addition, dye adsorption and photocatalytic properties of **1** and magnetic properties of **1–2** have been investigated.

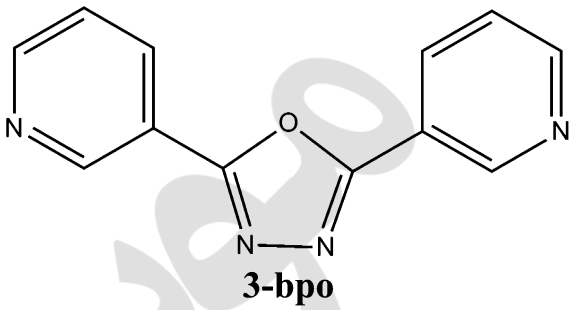

Scheme 1 Structure of the 3-bpo ligand used in this work.

Experimental

Materials and general methods

The 3-bpo ligand was synthesized according to the reported literature method.[17] Other reagents and solvents for synthesis were purchased from commercial sources, and used without further purification. C, H, and N elemental analyses were performed on an Elementar Vario EL III microanalyzer. The IR spectra were obtained on a Vertex70 Spectrum with KBr pellet in the 400–4000^{-1} region. Thermal stability studies were carried out on a TGA/DSC 1 STAR^e system under N_2 with a rate of 10 °C min^{-1}. Powder X-ray diffraction data were recorded on a MiniFlexII powder diffractometer with graphite monochromatized Cu-Kα radiation (λ = 1.54056 Å) (Scheme 1).

Optical diffuse reflectance spectra were measured on a PELambda 900 UV-Vis spectrophotometer with $BaSO_4$ plate as the reference. Photocatalysis of compound **1** was carried out with a 300 W Xe lamp as a visible light source and analyzed by UV-Visible spectroscopy. Magnetic measurements were performed using a commercial Quantum Design Physical Property Measurement System (PPMS) and Magnetic Property Measurement System (MPMS). Magnetic susceptibility was measured at 0.1 T or 0.5 T from 300 to 2 K and magnetization was measured at 2 K in an applied field from −8 to 8 T.

Synthesis of $[Cu(3\text{-bpo})(H_2O)(Mo_4O_{13})]{\cdot}3H_2O$ (1)

A mixture of $Cu(Ac)_2{\cdot}H_2O$ (100.0 mg, 0.5 mmol), 3-bpo (40.0 mg, 0.177 mmol), $(NH_4)_6Mo_7O_{24}{\cdot}4H_2O$ (150.0 mg, 0.121 mmol) was dissolved in 10 ml deionized water at room temperature. After the pH value of the mixture was adjusted to about 3.0 with 2 M HCl, the reaction suspension was transferred and sealed in a glass vial, placed at 95 °C under autogenous pressure for 3 days, and then cooled slowly to room temperature over two days, resulting in green crystals of **1**. The crystals were filtered, washed with H_2O and dried in open air (90% yield based on Mo). Anal. Calcd (Found %) for **1**: C, 15.10(15.15); H, 1.88(1.77); N, 5.87(5.83). IR (KBr, cm^{-1}): 3427 (m), 3093(w), 2966(w), 1623(m), 1557(w), 1483(w), 1423(m), 1262(m), 1102(m), 962(s), 895(s), 801(s), 694(s), 601(s).

Synthesis of $[Cu_2(3\text{-bpo})_2(Mo_6O_{20})]$ (2)

A mixture of $Cu(Ac)_2{\cdot}H_2O$ (100.0 mg, 0.5 mmol), 3-bpo (40.0 mg, 0.177 mmol), $(NH_4)_6Mo_7O_{24}{\cdot}4H_2O$ (150.0 mg, 0.121 mmol) was dissolved in 5 mL deionized water and 5 mL ethanol at room temperature. After the pH value was adjusted to about 4.2 with 2.0 M HCl, the reaction suspension was sealed in a Parr Teflon lined stainless steel vessel (20 mL), kept

at 110 °C under autogenous pressure for 3 days, and then cooled slowly to room temperature. Green crystals of **2** were filtered, washed with H_2O, and then dried in open air (60% yield based on Mo). Anal. Calcd (Found %) for **2**: C, 19.52(19.45); H, 1.35(1.19); N, 7.59(7.65). IR (KBr, cm^{-1}): 3454(w), 3107(w), 1616(m), 1557(m), 1489(m), 1416(m), 1202(m), 1096(m), 1055 (w), 1022(w), 948(s), 888(s), 795(s), 708(s), 641(s), 560(s).

X-ray crystallography

Single-crystal X-ray diffraction data of complex **1** were recorded on a MicroMax 007 diffractometer equipped with a CCD detector using Mo-Kα monochromatized radiation (λ = 0.71073 Å) at 173 K, while that of **2** were collected on an Agilent Technologies Super-Nova diffractometer equipped with Atlas CCD detector using monochromated Cu Kα radiation (λ = 1.54184 Å) at 293 K. The data were corrected for absorption using multiscan technique as implemented in SADABS. The structures were solved by direct methods and refined by full-matrix least-squares on F^2 using the SHELXTL software package.[18] A "ISOR" restrain was performed on one carbon atom with NPD problems in the crystal structure of **1**, and all other non-hydrogen atoms in both structures were refined with anisotropic parameters. All H atoms on carbon atoms were generated geometrically and refined in the riding model using isotropic displacement parameters, while the H atoms on lattice and coordinated water molecules of **1** were found from *E*-map and then refined with a O···H distance restraining parameter of 0.84 Å. Crystallographic data and structure refinements for complexes **1** and **2** are summarized in Table 1. Selected bond distances and angels are listed in Table S1 (ESI†). The CCDC reference numbers are 1003521 for **1** and 1003522 for **2**.

Table 1 Crystal data and structure refinements for complexes **1–2**

	1	**2**
Empirical formula	$C_{12}H_{16}CuMo_4N_4O_{18}$	$C_{12}H_8CuMo_3N_4O_{11}$
F_w	951.59	735.59
Space group	$P\bar{1}$	$P\bar{1}$
a (Å)	8.252(6)	8.2951(4)
b (Å)	9.073(6)	9.1416(6)
c (Å)	16.414(11)	13.2695(7)
α (°)	88.681(9)	109.205(6)
β (°)	80.237(9)	93.720(4)
γ (°)	70.809(8)	109.834(5)
V (Å^3)	1143.1(14)	876.04(9)
Z	2	2
d_{calcd} (g cm^{-3})	2.765	2.789
μ (mm^{-1})	3.148	19.266
F (000)	914	702
Reflections collected	11 254	7287
Unique reflections (R_{int})	5134 (0.0399)	3632(0.0368)
Restraints/parameters	16/373	0/280
GOF on F^2	1.092	1.019
R_1,[a] wR_2 [b] ($I > 2\sigma(I)$)	0.0710, 0.2451	0.0315, 0.0775
R_1, wR_2 (all data)	0.0774, 0.2492	0.0419, 0.0849
Max, min peaks (e Å^3)	2.029, −1.373	0.880, −0.958

[a] $R_1 = \sum||F_o| - |F_c||/\sum|F_o|$. [b] $wR_2 = \{\sum[w(F_o^2 - F_c^2)^2]/\sum[w(F_o^2)^2]\}^{1/2}$.

Dye molecule adsorption experiments for 1

Adsorption experiments included adsorption equilibrium experiments, adsorption kinetic experiments, selective adsorption experiments, and desorption experiments. As-synthesized crystals were dispersed into the dye solution at room temperature in a flask by simultaneous stirring. At a given time interval, the concentrations of dyes were measured with UV-vis spectra at the maximum absorbance of each dye (664 nm, 464 nm, 554 nm, 581 nm for MB, MO, RhB and methyl violet, respectively). The details of each type of experiments are given in the ESI.†

MO and MB photodegradation using 1

As-synthesized crystals of **1** (80.0 mg) and hydrogen peroxide (30%, 2.0 mL) were dispersed in an aqueous solution of methyl orange (MO, 20 mg L^{-1}, 100 mL) or methylene blue (MB, 20 mg L^{-1}, 100 mL) by simultaneous stirring, and then irradiated with a 300 W Xe lamp as a visible light source. Sample aliquots were withdrawn from the reactor intermittently during the illumination, and evaluated by measuring the absorbance of MO or MB solution after a regular interval visible light irradiation. For comparison, blank experiments in the absence of **1** were also performed. Owing to a significantly selective adsorption for methylene blue (MB), different amounts of peroxide were used to investigate such effects on the photodegradation of MB molecules in solution and the release of adsorbed MB on **1**.

Structural description

Crystal structure of 1. Complex **1** crystallizes in the triclinic space group $P(\bar{1})$. There are four unique Mo atoms in the asymmetric unit of **1** and each resides in a square-pyramidal coordination geometry formed with one double-bond oxygen in the apex and four single Mo–O bonds in the base (Fig. 1a). However, the Mo1, Mo3 and their central-symmetric sites are weakly bonded to a N atom (Mo–N, 2.648–2.687 Å) from the oxadiazole moiety of 3-bpo ligands and edge-shared into a Z-shaped $\{Mo_4O_{13}\}$ unit, while the Mo2, Mo4 and their central-symmetric sites are weakly bonded to a lattice μ_2-H_2O molecule (Mo–O, 2.642–2.635 Å) and edge-shared into an anti-Z-shaped $\{Mo_4O_{13}\}$ unit (Fig. 1b). Interestingly, the two kinds of $\{Mo_4O_{13}\}$ units can be viewed as the half split of centro-symmetric β-$[Mo_8O_{26}]^{4-}$, and are extended into 1D infinite zigzag chains $\{Mo_4O_{13}\}_n$ through sharing μ_2-O corners (Fig. 1c). Every Z-shaped $\{Mo_4O_{13}\}$ unit provides four oxygen sites while the anti-Z-shaped unit prepares two oxygen sites to coordinate Cu (II) ions. As a result, adjacent $\{Mo_4O_{13}\}$ chains are further bridged by Cu(II) ions into a 2D inorganic layer (Fig. 1c).

As shown in Fig. 2a–c, each 3-bpo ligand acts as a tetradentate linkage, in which two pyridyl N-donors are coordinated to Cu(II) ions, while two oxadiazole N-donors are weakly bonded to Z-shaped $\{Mo_4O_{13}\}$ units. As a result, 3-bpo ligands are located on either side of an inorganic layer and serve as arched footbridges to link Cu(II) ions in the layer. All Cu(II) ions in the hybrid layer exhibit a slightly distorted

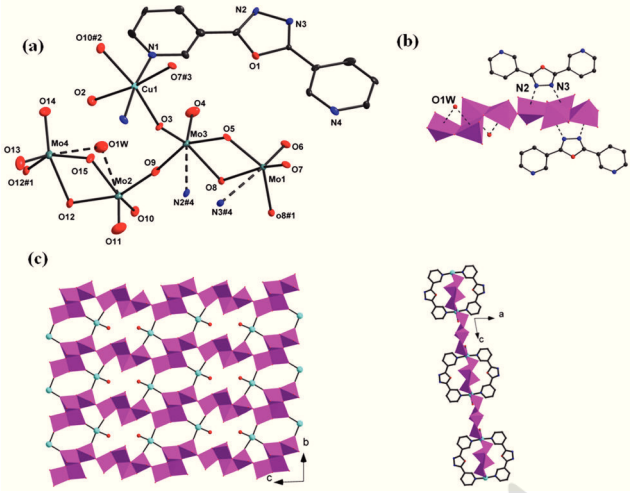

Fig. 1 (a) The asymmetric unit and coordination environments around metal ions in **1**. Symmetric codes: #1 – *x*, 1 – *y*, 1 – *z*; #2*x*, 1 + *y*, *z*; #3 – *x*, 2 – *y*, 1 – *z*; #4 –1 + *x*, *y*, *z*. (b) Z-shaped and anti-Z-shaped $\{Mo_4O_{13}\}$ units in **1**; (c) $\{Mo_4O_{13}\}_n$ chains connected by Cu(II) ions into an inorganic layer (organic ligands coordinated to Cu(II) are omitted for clarity) (left), a view along *b*-axis showing 3-bpo ligands on either side of the inorganic layer (right). (All solid lines represent coordination bonds, while the dashed lines represent the weak interactions between Mo and lattice water molecules or oxadiazole nitrogens).

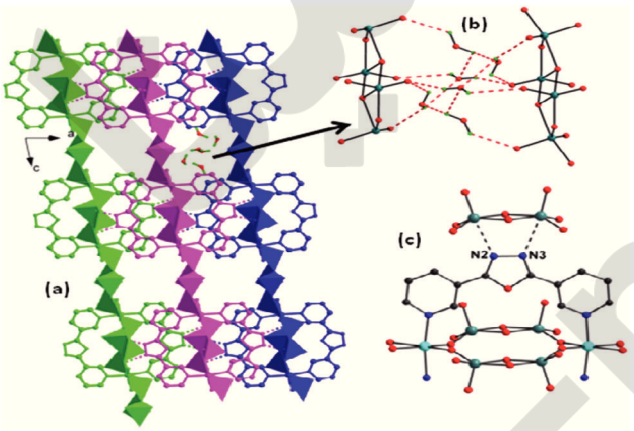

Fig. 2 (a) 3D supramolecular framework of **1**, with channels occupied by water molecules (all H on ligands are omitted for clarity); (b) the interactions of water molecules with anti-Z-shaped $\{Mo_4O_{13}\}$ units in **1** (O, red, H, green). (c) The coordination mode of the 3-bpo ligand and weak Mo–N bonds in **1**.

octahedral coordination geometry with normal bond distances (*i.e.* Cu–O, 2.091(9)–2.197(9) Å, Cu–N, 1.981(8)–1.985(11) Å) and bond angles (see Table S1†).[19]

Furthermore, adjacent hybrid layers are connected *via* weak Mo–$N_{oxadiazole}$ bonds (Mo–N, 2.648(8)–2.687(8) Å) into a 3D supramolecular framework with 1D channels along the *b*-axis. Interestingly, water molecules in channels are hydrogen-bonded together to form water clusters, which are further interacted with the host framework *via* either O–H···O bonds or weak Mo–O1W bonds (Mo–O, 2.641(4)–2.635(4) Å). On considering the weak Mo–N and Mo–O1W bonds, the coordination geometries of Mo atoms in **1** may be also described as axially elongated distorted octahedra.

Crystal structure of 2

Single-crystal X-ray diffraction analysis revealed that complex **2** crystallizes in the triclinic $P(\bar{1})$ space group, and its structure is constructed from a 2D bimetallic oxide network $[Cu(3\text{-bpo})(Mo_6O_{20})_{1/2}]_n$ with the 3-bpo ligands located on either side of the layer. As shown in Fig. 3a, there are three crystallographically independent Mo atoms in the asymmetrical unit of **2**, in which both Mo2 and Mo3 are coordinated with five oxygens in a square-pyramidal geometry and have two short Mo–O bonds (1.679(4)–1.747(4) Å), two medium Mo–O bonds, (1.907(4)–1.941(3) Å) and one long Mo–O bond, (2.114(3)–2.171(4) Å), while Mo1 tetrahedrally coordinates two μ_2-oxygens and two *t*-oxygens (Mo–O, 1.707(4)–1.856(4) Å). Mo2, Mo3 and their central-symmetric sites are edge-shared to form an anti-Z-shaped $\{Mo_4O_{13}\}$ cluster core, which is structurally analogous to that observed in **1** and the 1D pyridinium isopolymolybdate.[20] Two MoO_4 tetrahedra are attached *via* corner-sharing to endpoints of the anti-Z-shaped $\{Mo_4O_{13}\}$ moiety, forming an unprecedented "S"-shaped hexamolybdate $[Mo_6O_{20}]^{4-}$ anion completely different from previously reported hexamolybdates.[15,16] As illustrated in Fig. 3b, each hexamolybdate $[Mo_6O_{20}]^{4-}$ offers eight oxygens to be coordinated by six Cu(II) ions. In turn, each Cu(II) ion links three hexamolybdate anions. The interconnection of Cu(II) ions and hexamolybdate anions *via* corner-sharing oxygens affords a 2D (3,6)-connected

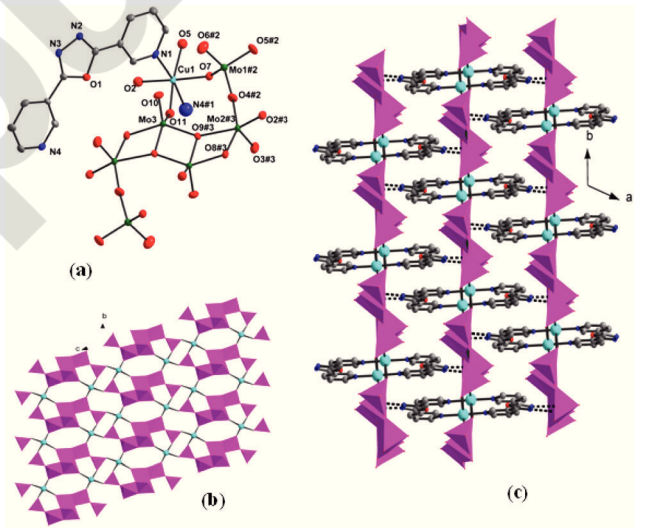

Fig. 3 (a) The asymmetric unit and $\{Mo_6O_{20}\}$ building units in **2**; (b) $\{Mo_6O_{20}\}$ units connected *via* Cu(II) ions into an inorganic layer in **2** (organic ligands coordinated to Cu(II) are omitted for clarity); (c) a view of 3D supramolecular framework showing 3-bpo ligands on either side of layers and weak Mo–$N_{oxadiazole}$ bonds (dashed lines) in **2** (symmetry code: #1, 1 – *x*, 1 – *y*, –*z*; #2, 1 – *x*, 1 – *y*, 1 – *z*;#3, *x*, *y* – 1, *z*).

inorganic layer (Fig. 3b). Interestingly, all Cu(II) ions in the layer are completely co-planar, and neighbouring Cu(II) ions exhibit two types of Cu···Cu separations. The short Cu···Cu separation (5.576 Å) is only bridged by two MoO_4 tetrahedra, while the longer one (7.973 Å) is bridged by two halves of $\{Mo_4O_{13}\}$ moieties and two 3-bpo ligands.

The 3-bpo ligands exhibit the same coordination mode as that observed in **1**. That is to say, 3-bpo ligands located on either side of the inorganic layers of **2** bridge Cu(II) ions *via* pyridyl N-donors, and as a result, each Cu(II) site in the layer exhibits a slightly distorted octahedral coordination geometry defined by four oxygens from three $[Mo_6O_{20}]^{4-}$ anions and two pyridyl N from two 3-bpo ligands. It should be noted that the axial Cu–O distances (2.326(3)–2.415(4) Å) are significantly longer than the equatorial distances of Cu–O (1.981(4)–1.984 (4) Å) and Cu–N bonds (2.008(4)–2.010(5) Å), owing to Jahn–Teller effect of Cu (II) ions. Similarly as observed in **1**, adjacent bimetallic layers are connected into 3D supramolecular framework (Fig. 3c) through weak Mo–$N_{oxadiazole}$ bonds (2.600(2)–2.669(6) Å).

Discussion

The amount and type of initial reactant in compounds **1** and **2** are completely the same as each other. However, different ambient conditions, such as, temperature, pressure, pH value, lead to different products which mainly differ in inorganic building blocks preparing for inorganic-polyoxometalates layers as well as their properties. But many similarities also exist as follows: First, the networks in two complexes differ in structure but resemble in constitute. In detail, they are both inorganic layers formed by copper ions and polyoxometalates anions. Second, the coordination mode of the 3-bpo ligand is completely same as the tetra-dentate linkage. Third, they are both polyoxometalate-organic supermolecules by weak Mo–N interactions from adjacent layers. Therefore, strictly controlling reaction conditions seem to be critical to synthesize functional-polyoxometalates materials.

Optical absorption spectra, TGA analysis and PXRD characterization of 1 and 2

Complexes **1** and **2** exhibit similar IR spectroscopy characteristics (see Fig. S1†), and the absorption bands can be divided into the following regions: (1) the moderately strong and broad band around 3400 cm^{-1} for **1** corresponding to the O–H stretching vibrations of hydrogen-bonded water molecules; (2) 3000–2800 cm^{-1} and 1620–1080 cm^{-1} attributed to the different types of stretching vibrations of organic ligands; (3) 1000–850 cm^{-1} mainly assigned to the Mo–O terminal stretching; and (4) 750–500 cm^{-1} assignable to the Mo–O–Mo bridge stretching (the vibrations of the Mo–O–Cu bonds may be also located in this last region). The measurement of UV-Vis diffused reflectance spectra of **1** and **2** at room temperature (see Fig. S2 and S3†) revealed an optical gap of *ca.* 2.9 eV, indicating that both complexes are underlying semi-conductor materials. To study the thermal stability of the complexes **1** and **2**, TGA measurements were carried out under a flow of N_2. For complex **1**, two distinct steps of weight loss are observed; the first one occurring at a temperature of 30–110 °C corresponds to the release of all lattice and coordinated water molecules (calc. 7.8%, found 7.5%), followed by a long platform until 320 °C after which the hybrid framework starts to decompose (Fig. S4†). Upon heating, complex **2** shows no obvious weight loss before the decomposition of framework, indicating no lattice solvent molecules in the structure, which is consistent with the single-crystal structure of **2**. As shown in Fig. S5,† the measured XRPD patterns of **1** and **2** are in good agreement with the ones simulated from single-crystal X-ray data, confirming the phase purities of both complexes.

Photocatalytic properties of 1

It is well known that many POMs and POM-based hybrid materials are efficient photocatalysts in the degradation of organic dyes.[21,22] Because of its structural features (1D channels existing in the 3D supramolecular framework) and narrow optical gap (*ca.* 2.9 eV, as revealed by the measurement of UV-Vis diffused reflectance spectra), complex **1** was chosen as a photocatalyst candidate to investigate the photodegradation of methyl orange (MO) and methylene blue (MB), which are common environment pollution sources difficult to be degraded. After dispensing the crystalline solids of **1** into the MO solution and the addition of a suitable quantity of H_2O_2, the reaction mixture was stirred and irradiated with 300 W Xe lamp as the visible light source. The decomposition of MO was monitored by the characteristic absorption peak of MO at 464 nm.

As shown in Fig. 4a, the characteristic adsorption peaks of MO solution are decreased obviously with increasing reaction time. The calculations revealed that the conversion of MO reaches up to 96.19% within two hours (Fig. 4b). In comparison, the absorption peaks of MO in the absence of **1** show no obvious change, and the degradation of MO is less than 10%. In addition, successive photocatalytic experiments were performed with the solids recycled from the reaction suspension by simple filtration, and similar results were obtained, showing that the activity of the recovered catalyst does not obviously decrease even after three cycles (Fig. S6†). Further, the PXRD patterns of **1** after degradation of MO are nearly identical to the simulated one from single-crystal structure (Fig. S7†), indicating that the framework structure remains unchanged. These above results suggest that complex **1** is a good heterogeneous photocatalyst in the degradation of MO organic dye. Similarly, photodegradation experiments were also designed for methylene blue (MB). As shown in Fig. 4c, it was observed that after 2 hours visible light irradiation the C/C_0 decreased close to zero in the presence of complex **1**, while that of the blank experiment without complex **1** decreased to 0.423, indicating that complex **1** also plays a certain degree of catalytic role in the photodegradation of MB.

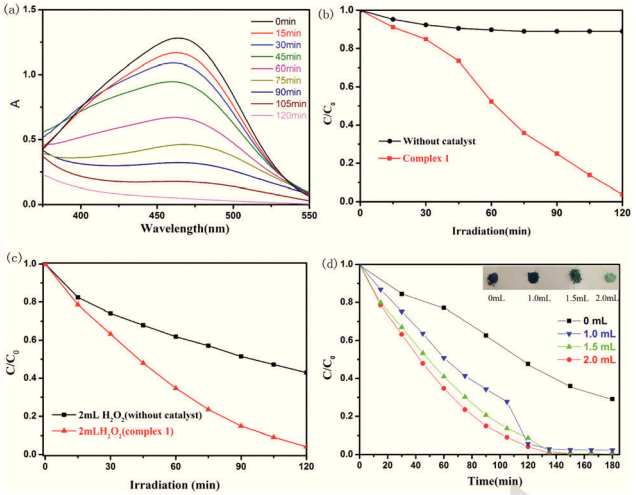

Fig. 4 (a) UV-Vis absorption spectra of the MO solution during the decomposition reaction in the presence of **1** under visible light irradiation. (b) Changes in C/C_0 plots of MO solution *versus* reaction time without a catalyst and in the presence of **1**. (c) Changes in C/C_0 plots of MB solution *versus* reaction time without a catalyst and in the presence of **1**. (d) Changes in C/C_0 plots of MB solution *versus* reaction time in the presence of different amounts of peroxide (0–2.0 mL) and the same amount of **1** under visible light irradiation. In all experiments, starting concentration of MO or MB, 20.0 mg L^{-1}, volume, 100 mL, complex **1** were used, 80 mg.

Dye molecule selective absorption on 1

In recent decades, much attention has been paid to applying POMs and related composites in photocatalytic degradation of organic dyes. However, some complexes exhibit poor degradability due to their structural limits. Thus, from the recycling point of view, it is more attractive and challenging to explore the capture ability to separate different organic dyes using POM composites. During the performance of photodegradation experiments of MB, it was observed that once the amount of MB solution (20 mg L^{-1}, 100 mL) and sample **1** (80 mg) were defined, the colour of the final powder solid recycled by filtration varied from a dark blue to green, upon the amount of hydrogen peroxide (*i.e.* 0, 1.0, 1.5 and 2.0 mL) used in the reaction (Fig. 4d). When the amount of peroxide was controlled at 2.0 mL, C/C_0 declined close to zero after 3 hours, and the colour of the solid obtained by filtration was green, same as the colour of as-synthesized crystals of **1**. However, if the amount of peroxide (*i.e.* 1.0 mL, and 1.5 mL) was less than 2.0 mL, the colour of the recycled solid was blue, and the lesser the dosage of peroxide, the deeper the colour of the recycled solid (Fig. 4d), indicating that complex **1** can further effectively absorb MB molecules after the consumption of peroxide as an oxidant to result in the concentration of MB solution finally close to zero. In fact, in the absence of peroxide (0 mL), the C/C_0 of MB solution can be decreased to 0.29 after 3 hours, and the recycled solid was deep blue, further confirming the adsorption ability of MB molecules on **1**. To fully evaluate the adsorption ability of methylene blue (MB) on complex **1**, a certain amount of **1** (5 mg or 10 mg) was dispensed into 100 ml MB solution with different concentrations (5–100 mg L^{-1}) under stirring in the dark at room temperature, and the concentrations of MB solution at a given time interval were monitored with the UV-Vis spectrum until the concentration was not changed. The specific adsorbed amount of MB was calculated according to the equation: $Q_e = V(C_0 - C_e)/m$ (C_0 and C_e are the initial and the equilibrium liquid-phase concentrations of MB (mg L^{-1}), respectively, m is the amount of adsorbent (g), and V is the volume of the solution). It was found that the uptake of MB on **1** increases almost linearly with the dye concentration in the low concentration region (Fig. 5a), and reaches the maximum uptake of 1184.4 mg g^{-1}, which is significantly higher than the values reported for POM composites $H_3PW_{12}O_{40}$@ZIF-8 (810 mg g^{-1}),[23] $PW_{11}V$@MIL-101 (371 mg g^{-1})[24] and $H_3PW_{12}O_{40}$@Mn^{III}-porphyrin (10.5 mg g^{-1}),[25] the commercial active carbon (135 mg g^{-1})[26] and graphene oxide (GO) sponges (387 mg g^{-1}).[27]

Besides the uptake capacity, we studied influence factors on the adsorption rate of MB on **1** *via* the following experiment routes: (**A**) crystals as-synthesized were statically placed in the MB solution without any disturbance (no stirring); (**B**) crystals were ground into powder and placed in the MB solution without any disturbance; (**C**) crystals as synthesized were added in the MB solution and stirred; (**D**) crystals were ground into powder, dispensed in the MB solution and stirred. The

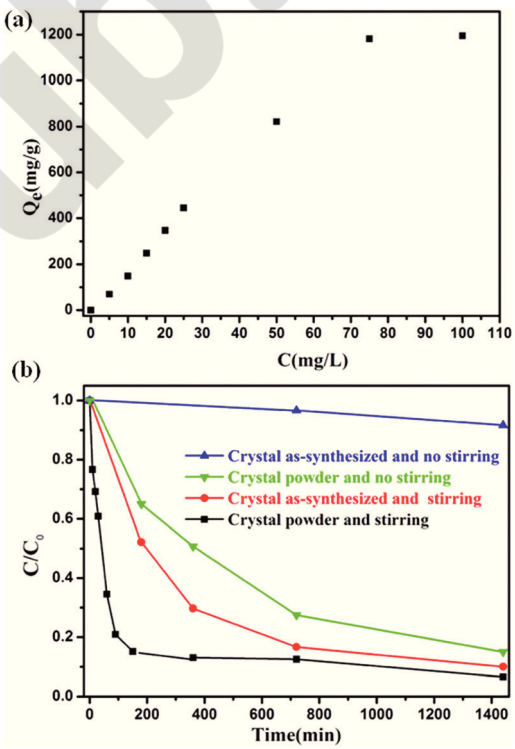

Fig. 5 (a) Adsorption isotherm of MB on complex **1** at 298 K. (b) Comparison of adsorption rates and uptake using different routes (starting concentration 10 mg L^{-1}, volume 100 mL, and mass of absorbent 5.0 mg).

same starting conditions (5.0 mg complex **1**, 10 mg L^{-1} 100 mL aqueous solution of MB) were used in routes **A–D**. As shown in Fig. 5b, within 60 minutes complex **1** in route **D** can absorb more than 65% of MB molecules present in the solution, while it takes routes **A–C** 720, 360 and 180 minutes, respectively, to reach their adsorbed MB percent of 3.7, 49.2 and 47.8, respectively.

After 24 hours in route **D**, it reaches the adsorption equilibrium, and absorbs 93.4% MB from the solution, which is significantly higher than the values for routes **B** (85.1%) and **C** (90.0%), and almost ten times that for route **A** (9.4%). The above results show that both the size of absorbent particles and whether stirring the MB solution have a great influence on uptake and adsorption rate, and it displays an order of uptake and adsorption rates: **A** < **B** < **C** < **D**.

The absorption selectivity of complex **1** is examined by dispensing crystalline powder (50 mg) of **1** into an aqueous solution (100 ml, 10 mg L^{-1}) of MB, methyl orange (MO), methyl violet (MV) or rhodamine B (RhB) under stirring in the dark, and determining the concentrations of dye solution at given intervals by the UV-Vis adsorption spectra. These dye molecules have different sizes and charges: the positively charged MB and MV with similar molecule sizes, the negatively charged MO, and cationic RhB with a larger molecule volume. From Fig. 6, it can be clearly seen that complex **1** has different adsorption ability towards different organic dyes. After 24 hours, complex **1** can effectively absorb 91.0% MB and 92.1% MV from the dye solution, which are about 7.3 times that for RhB (12.5%), while the removal percent of MO is less than 0.6%. The adsorption selectivity of **1** is further investigated by applying a binary mixture of MB/RhB (positively charged with different sizes) or MB/MO (similar sizes with different electronegativity). As shown in Fig. 7, complex **1** can selectively capture MB molecules from the corresponding binary mixture after 48 hour, along with the UV-Vis adsorption characteristic peak of MB almost disappearing, and leaving the characteristic peak of RhB or MO. The adsorption selectivity of **1** towards organic dyes is obviously related to structures of both **1** and dye molecules. Firstly, the pore in complex **1** has partial negative charges due to the existence of polyoxometalate units around which negative oxygens are present. From this point of view, there are relatively strong forces between small cationic dye molecules and the host framework, and complex **1** therefore demonstrates a good adsorption property toward MB and MV. However, the uptake of cationic RhB is relatively low due to its large molecule volume which may cause a steric hindrance between RhB molecules and active adsorption sites on **1**. Although MO molecules have similar molecule size as MB, a very little uptake capacity was observed for MO as the negative charge of this dye molecule causes charge repulsion between MO molecules and active adsorption sites on **1**.

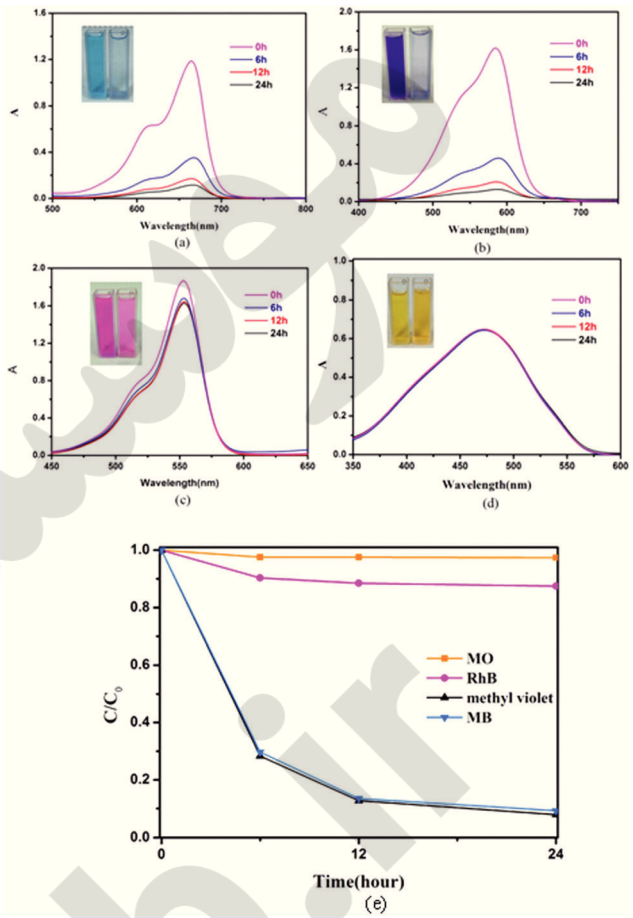

Fig. 6 The adsorption activity of complex **1** (50.0 mg) toward different dye aqueous solutions (solution concentrations, 10 mg L^{-1}, solution volumes, 100 ml): (a) MB (b) methyl violet (c) RhB (d) MO. (e) Dye concentration changes in (a)–(d) along with adsorption time.

Release of MB absorbed on 1

To test the release ability of MB adsorbed, a fresh sample (20 mg) of **1** was immersed in an aqueous solution (100 mg L^{-1}, 300 mL) of MB for sufficient time. Upon loading of MB in **1** (1168 mg g^{-1}), the deep blue powder solids were obtained by filtration and rapidly washed by pure water (300 mL) in a beaker under stirring. The colour of aqueous solution gradually changed from colourless to light blue and the release process was monitored and calculated by liquid phase UV-vis spectra. Fig. 8a shows that desorption equilibrium was almost and quickly achieved within 30 minutes. However, only about 18.5% of the MB molecules can be released into the solution, and the colour of the solid obtained after MB release equilibrium was still deep blue, which indicates that MB molecules have relatively strong interactions with **1**, and most of MB molecules remain on **1**. As shown in Fig. 8b, the concentration of MB molecules released into solution reaches a maximum value after about 30 min in the presence of peroxide and under irradiation of visible light, and then gradually decreases through photodegradation. If the amount of peroxide added is adequate, all MB molecules absorbed on **1** can be completely released and degraded, and finally the solid obtained by filtration recovers its original color (green); and as more peroxide was added, the quicker the MB adsorbed on **1** degraded.

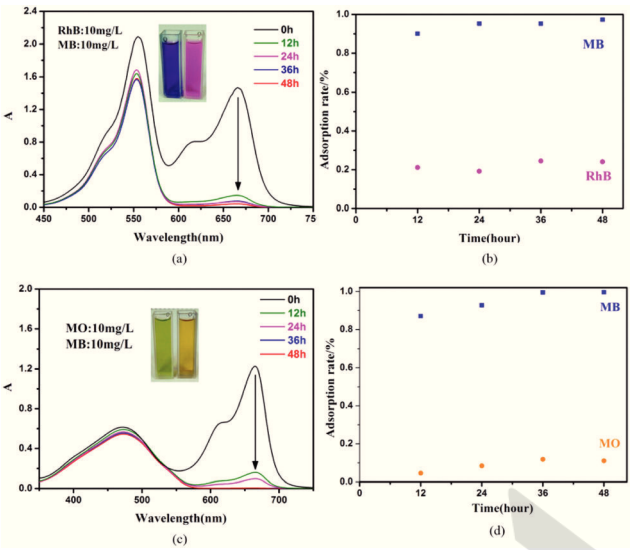

Fig. 7 (a) The selective adsorption capability of **1** toward the mixed solution of RhB and MB; (b) the removal percents of RhB and MB in the mixed solution; (c) the selective adsorption capability of **1** toward the mixed solution MO and MB. (d) The removal percents of MO and MB in the mixed solution. The starting concentration of each dye component in the binary mixture is 10 mg L^{-1}.

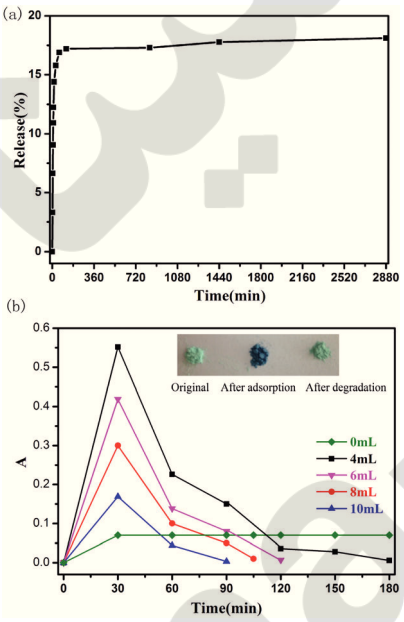

Fig. 8 (a) MB molecule release in pure water at room temperature. (b) Release and photodegradation of absorbed MB molecules in the presence of H_2O_2.

However, here it requires twice the amount of peroxide to degrade the same amount of MB than that used in the above-mentioned photodegradation of MB. The reason may be that desorption of MB is a slow process and the amount of peroxide required is more.

Magnetic properties of 1–2

Magnetic susceptibilities of **1** were measured under an applied field of 5 kOe in the temperature range from 300 to 2 K. As shown in Fig. 9, susceptibility continuously increases with lowering the temperature and the $\chi_m T$ value at room temperature is 0.457 cm^3 mol^{-1} K, slightly higher than the expected value of 0.375 mol^{-1} K for one Cu(II) (S = 1/2, g = 2). In addition, a typical Curie–Weiss behaviour is observed, giving the Curie constant C = 0.45 cm^3 mol^{-1} K and the Weiss constant θ = −0.22 K, indicating obvious paramagnetic phenomenon (Fig. S8†).

Magnetic susceptibilities of **2** were measured under an applied field of 1 kOe in the temperature range from 300 to 2 K. As shown in Fig. 10a, the susceptibility continuously increases with lowering the temperature and a sharp peak is observed at about 5 K, indicating characteristics of antiferromagnetic (AF) ordering. The $\chi_m T$ value at room temperature is 0.422 cm^3 mol^{-1} K, slightly higher than the expected value of 0.375 mol^{-1} K for one Cu(II) (S = 1/2, g = 2), maintains a constant upon lowering the temperature until 50 K, and then suddenly drops to a value of 0.04 cm^3 mol^{-1} K at 2 K. This behaviour indicates the occurrence of antiferromagnetic interactions between Cu^{II} centers.

Furthermore, a typical Curie–Weiss behaviour is observed in the temperature range of 12–300 K, giving the Curie constant C = 0.41 cm^3 mol^{-1} K and the Weiss constant θ = −1.38 K (Fig. S9†). The negative Weiss constant also suggests that the dominative interactions between Cu^{2+} ions are antiferromagnetic interactions. As shown in Fig. 10b, the magnetization (M) as a function of applied field (H) at 2 K shows a linear increase of magnetization in the range of 0–2.5 T with increasing field, indicating a characteristic AF ground state. An abrupt increase is observed at the field of ~4 T, indicating the appearance of a spin-flop transition. The spin-flop transition field is about 5.8 T determined by the curves of dM/dH (Fig. 10b, insert). The magnetization value at 8 T is 0.83$N\beta$ close to the saturation value of 1.0$N\beta$ for one Cu^{2+} ion with S = 1/2, showing that the spins enter nearly into the ferromagnetic state. No hysteresis features are seen in increasing and decreasing field regimes (Fig. S10†). Magnetic susceptibilities

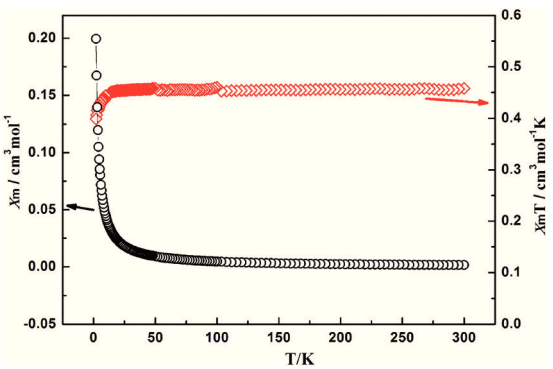

Fig. 9 Temperature dependence of χ_m and $\chi_m T$ of **1**.

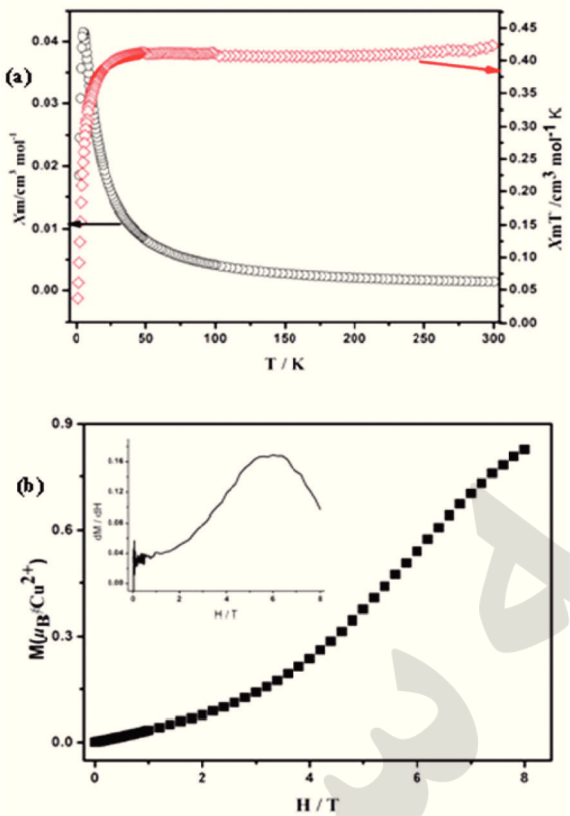

Fig. 10 (a) Temperature dependence of χ_m and $\chi_m T$ of **2**. (b) The field dependence of the magnetization at 2 K. Insert: the d*M*/d*H* derivative curve.

of **2** under different magnetic fields were also measured in the temperature range of 2–30 K. As shown in Fig. S11,† the peak gradually disappears with an increasing magnetic field, between 5.5 and 6.0 T, which is in good agreement with above magnetic data, confirming that the field-induced magnetic transition is spin-flop from AF to F phases.

Conclusions

In summary, we have synthesized two interesting 2D POM-based inorganic–organic hybrid materials under hydrothermal conditions. The $\{Mo_4O_{13}\}_n$ chains in **1** and unprecedented $[Mo_6O_{20}]^{4-}$ isopolyhexamolybdate anions in **2** are linked by octahedral Cu^{2+} ions into two-dimensional hybrid layers. Interestingly, 3-bpo ligands in both **1** and **2** are located on either side of layers and serve as arched footbridges to link Cu(II) ions in the layer *via* pyridyl N-donors, and at the same time connect these hybrid layers into 3D supramolecular frameworks *via* weak $Mo\cdots N_{oxadiazole}$ bonds. Another important point for **1** is that water clusters are filled in the 1D channels surrounded by isopolytetramolybdate units. In addition, dye adsorption and photocatalytic properties of **1** and magnetic properties of **2** have been investigated. The results indicated that complex **1** is not only a good heterogeneous photocatalyst in the degradation of MO and MB organic dyes, but also has high absorption capacity of MB and excellent ability to selectively capture MB from binary mixtures. All MB molecules absorbed on **1** can be completely released and photodegraded in the presence of adequate peroxide. The temperature dependence of magnetic susceptibility revealed that complex **2** exhibits antiferromagnetic ordering at about 5 K, and a spin-flop transition was observed at about 5.8 T at 2 K, indicating metamagnetic-like behaviour from antiferromagnetic to ferromagnetic phases.

Acknowledgements

This work was supported by the 973 key program of the MOST (2010CB933501, and 2012CB821705), the Chinese Academy of Sciences (KJCX2-YW-319, KJCX2-EW-H01), the National Natural Science Foundation of China (21373221, 21221001, 91122027, 51172232, 21403236) and the Natural Science Foundation of Fujian Province (2012J06006, 2011HZ0001-1, 2006L2005, 2009HZ0004-1, 2009HZ0005-1, 2007HZ0001-1).

Notes and references

1 (*a*) F. J. Ma, S. X. Liu, C. Y. Sun, D. D. Liang, G. J. Ren, F. Wei, Y. G. Ya and Z. M. Su, *J. Am. Chem. Soc.*, 2011, **133**, 4178; (*b*) X. F. Kuang, X. Y. Wu, R. M. Yu, J. P. Donahue, J. S. Huang and C. Z. Lu, *Nat. Chem.*, 2010, **2**, 461; (*c*) P. P. Zhao, Y. Leng, M. J. Zhang, J. Wang, Y. J. Wu and J. Huang, *Chem. Commun.*, 2012, **48**, 5721; (*d*) J. Ettedgui, Y. Diskin-Posner, L. Weiner and R. Neumann, *J. Am. Chem. Soc.*, 2011, **133**, 188; (*e*) S. T. Zheng, J. Zhang, X. X. Li, W. H. Fang and G. Y. Yang, *J. Am. Chem. Soc.*, 2010, **132**, 15102; (*f*) H. Y. An, E. B. Wang, D. R. Xiao, Y. G. Li, Z. M. Su and L. Xu, *Angew. Chem., Int. Ed.*, 2006, **45**, 904.

2 D. A. Judd, J. H. Nettles, N. Nerins, J. P. Snyder, D. C. Liotta, J. Tang, J. Ermolieff, R. F. Schinazi and C. L. Hill, *J. Am. Chem. Soc.*, 2001, **123**, 886.

3 (*a*) X. K. Fang, P. Kögerler, M. Speldrich, H. Schilder and M. Ludan, *Chem. Commun.*, 2012, **48**, 1218; (*b*) X. K. Fang, L. Hansen, F. Haso, P. C. Yin, A. Pandey, L. Engelhardt, I. Slowing, T. B. Liu, M. Luban and D. C. Johnston, *Angew. Chem., Int. Ed.*, 2013, **52**, 1; (*c*) J. M. C. Juan, E. Coronado and A. G. Arino, *Chem. Soc. Rev.*, 2012, **41**, 7464.

4 (*a*) B. Nohra, H. E. Moll, L. M. R. Albelo, P. Mialane, J. Marrot, C. Mellot-Draznieks, M. O'Keeffe, R. N. Biboum, J. Lemaire, B. Keita, L. Nadjo and A. Dolbecq, *J. Am. Chem. Soc.*, 2011, **133**, 13363; (*b*) X. L. Wang, Y. F. Bi, B. K. Chen, H. Y. Lin and G. C. Liu, *Inorg. Chem.*, 2008, **47**, 2442.

5 (*a*) J. Lü, J. X. Lin, X. L. Zhao and R. Cao, *Chem. Commun.*, 2012, **48**, 669; (*b*) J. Zhang, W. Li, C. Wu, B. Li, J. Zhang and L. X. Wu, *Chem. – Eur. J.*, 2013, **19**, 8129.

6 (*a*) D. R. Xiao, Y. Hou, E. B. Wang, S. T. Wang, Y. G. Li, L. Xu and C. W. Hu, *Inorg. Chim. Acta*, 2004, **357**, 2525;

(*b*) D. G. Allis, E. Burkholder and J. Zubieta, *Polyhedron*, 2004, **23**, 1145; (*c*) H. Y. Zang, K. Tan, W. Guan, S. L. Li, G. S. Yang, K. Z. Shao, L. K. Yan and Z. M. Su, *CrystEngComm*, 2010, **12**, 3684.

7 (*a*) W. G. Klemperer and W. Shum, *J. Am. Chem. Soc.*, 1976, **98**, 8291; (*b*) D. Hagrman, P. J. Zapf and J. Zubieta, *Chem. Commun.*, 1998, 1283; (*c*) D. G. Allis, E. Burkholder and J. Zubieta, *Polyhedron*, 2004, **23**, 1145.

8 (*a*) D. G. Allis, R. S. Raring, E. Burkholder and J. Zubieta, *J. Mol. Struct.*, 2004, **688**, 11; (*b*) Q. G. Zhai, C. Z. Lu, Q. Z. Zhang, X. Y. Wu, X. J. Xu, S. M. Chen and L. J. Chen, *Inorg. Chim. Acta*, 2006, **359**, 3875; (*c*) Z. C. Yue, H. J. Du, Y. Y. Niu and G. X. Jin, *CrystEngComm*, 2013, **15**, 9844; (*d*) L. J. Chen, C. Z. Lu, X. He, Q. Z. Zhang, W. B. Yang and X. H. Lin, *J. Solid State Chem.*, 2006, **179**, 2541; (*e*) R. S. Rarig Jr. and J. Zubieta, *Polyhedron*, 2003, **22**, 177.

9 (*a*) W. T. A. Harrison, L. L. Dussack and A. J. Jacobson, *Acta Crystallogr., Sect. C: Cryst. Struct. Commun.*, 1996, **52**, 1075; (*b*) K. Pavani and A. Ramanan, *Eur. J. Inorg. Chem.*, 2005, 3080.

10 L. Zhang, X. Kuang, X. Wu, W. Yang and C. Lu, *Dalton Trans.*, 2014, **43**, 7146.

11 W. Yang, C. Lu and H. Zhuang, *J. Chem. Soc., Dalton Trans.*, 2002, 2879.

12 D. Hagrman and J. Zubieta, *Chem. Commun.*, 1998, 2005.

13 (*a*) Z. L. Fang, J. G. He, Q. S. Zhang, Q. K. Zhang, X. Y. Wu, R. M. Yu and C. Z. Lu, *Inorg. Chem.*, 2011, **50**, 11403; (*b*) Z. L. Fang, R. M. Yu, X. Y. Wu, J. S. Huang and C. Z. Lu, *Cryst. Growth Des.*, 2011, **11**, 2546.

14 Z. Fang, W. Yang, J. He, K. Ding, X. Wu, Q. Zhang, R. Yu and C. Lu, *CrystEngComm*, 2012, **14**, 4794.

15 (*a*) L. J. Chen, X. He, C. K. Xia, Q. Z. Zhang, J. T. Chen, W. B. Yang and C. Z. Lu, *Cryst. Growth Des.*, 2006, **6**, 2076; (*b*) S. Takara, S. Ogo, Y. Watanabe, K. Nishikawa, I. Kinoshita and K. Isobe, *Angew. Chem., Int. Ed.*, 1999, **38**, 3051.

16 (*a*) Z. X. Li, H. Ma, S. L. Chen, Z. D. Pan, Y. F. Zeng, X. L. Xiu and X. H. Bu, *Dalton Trans.*, 2011, **40**, 31; (*b*) C. J. Zhang, C. H. Zhang, H. J. Pang, D. P. Wang, Q. J. Kong, X. D. Yang, F. Yao, Q. Tang, H. Y. Wang and Y. G. Chen, *J. Solid State Chem.*, 2010, **12**, 281.

17 F. Bentiss and M. Lagrenée, *J. Heterocycl. Chem.*, 1999, **36**, 1029.

18 (*a*) G. M. Sheldrick, *SHELXL97, Program for Crystal Structure Refinement*, University of Göttingen, Göttingen, Germany, 1997; (*b*) G. M. Sheldrick, *SHELXS97, Program for Crystal Structure Solution*, University of Göttingen, Göttingen, Germany, 1997.

19 (*a*) S. V. Radio, N. A. Melnik, E. S. Ivantsova and V. N. Baumer, *J. Struct. Chem.*, 2014, **55**, 879; (*b*) J. W. Zhao, J. L. Zhang, Y. Z. Li, J. Cao and L. J. Chen, *Cryst. Growth Des.*, 2014, **14**, 1467.

20 M. Michalec, K. Stadnicka and S. A. Hodorowicz, *Cryst. Res. Technol.*, 2007, **42**, 91.

21 (*a*) J. Lü, J. X. Lin, X. L. Zhao and R. Cao, *Chem. Commun.*, 2012, **48**, 669; (*b*) Y. Hu, F. Luo and F. F. Dong, *Chem. Commun.*, 2011, **47**, 761; (*c*) H. Lin and P. A. Maggard, *Inorg. Chem.*, 2008, **47**, 8044.

22 X. L. Wang, Q. Gao, A. X. Tian and G. C. Liu, *Cryst. Growth Des.*, 2012, **12**, 2346.

23 R. Li, X. Q. Ren, J. S. Zhao, X. Feng, X. Jiang, X. X. Fan, Z. G. Lin, C. W. Hu and B. Wang, *J. Mater. Chem. A.*, 2014, **2**, 2168.

24 A. X. Yan, S. Yao, Y. G. Li, Z. M. Zhang, Y. Lu, W. L. Chen and E. B. Wang, *Chem. – Eur. J.*, 2014, **20**, 6927.

25 C. Zou, Z. J. Zhang, X. Xu, Q. I. Gong, J. Li and C. D. Wu, *J. Am. Chem. Soc.*, 2012, **134**, 87.

26 The national standard of the People's Republic of China: wooden granular active carbon for water purification. GB/T13803.2-1999.

27 F. Liu, S. Chung, G. Oh and T. S. Seo, *ACS Appl. Mater. Interfaces*, 2012, **4**, 922.

Supporting Information

Two novel POM-based inorganic-organic hybrid compounds: synthesis, structures, magnetic properties, photodegradation and selective absorption of organic dyes†

Xuejing Dui,[a,c] Wenbin Yang*,[a,b] Xiaoyuan Wu,[a,b] Xiaofei Kuang,[a,b] Jianzhen Liao,[a,c] Rongmin Yu,[a,b] and Canzhong Lu*[a,b]

a: Key Laboratory of Design and Assembly of Functional Nanostructures, Fujian Institute of Research on the Structure of Matter, Chinese Academy of Sciences;

b: Fujian Provincial Key Laboratory of Nanomaterials, Fujian Institute of Research on the Structure of Matter, Chinese Academy of Sciences;

c: University of Chinese Academy of Sciences, Beijing, 100049, China.

Corresponding author: Prof. Can-Zhong Lu and Wen-Bin Yang

E-mail: czlu@fjirsm.ac.cn and ywb@fjirsm.ac.cn

Phone: +86-591-83705794

Fax: +86-591-83714946

Experiments

Optical band gaps

The UV-vis absorption spectra of compounds **1** and **2** were performed in the crystalline state at room temperature (Figure S1a). Some inorganic-organic hybrid materials based on inorganic polyoxometalates units have been testified to be good semiconductors.[1] So we investigated the conductivities of compounds **1** and **2**. The measurements of diffuse reflectivity for powder samples were carried out to obtain their band gaps (E_g). The E_g values are determined as the intersection point between the energy axis and the line extrapolated from the linear portion of the adsorption edge in a plot of Kubelka-Kunk function F versus energy E($F=(1-R)^2/2R$).[2] As shown in Figure S1b, the E_g value of both complexes are about 2.9 eV, indicating that both **1** and **2** are underlying semi-conducting materials.

Methylene blue (MB) Adsorption experiments

Adsorption equilibrium experiments were carried out by adding 5mg or 10mg as-synthesized crystals of complex **1** into 100ml MB solution with different concentration (5-100 mg L^{-1}) at room temperature in dark under stirring. After several days, the concentration was not changed and the final value was defined by UV-vis spectrometer at 664 nm.

The specific adsorbed amount of MB was calculated according to the equation:

$Q_e=V\ (C_0-C_e)/m$, where C_0 and C_e are the initial and the equilibrium liquid-phase concentration of MB (mg L^{-1}), m is the amount of adsorbent (g), and V is the volume of the solution (L). The results are shown in Figure 5a in text.

Adsorption kinetic experiments

As-synthesized crystals (5.0 mg) of complex **1** were dispersed into the MB solution (10 mg L^{-1}, 100 mL) with stirring or without any disturbance (no stirring). At given time intervals, the change of the concentration of the MB solution was monitored using UV-vis spectra at 664 nm. The results are shown in Figure 5b in text.

Dye adsorption selective kinetic experiments.

As-synthesized crystals of complex **1** (50mg) was added into the aqueous solution (10 mg L^{-1}, 100 mL) of MB, methy violet (MV), MO and RhB, respectively, at room temperature under stirring. At given time intervals, the change of the concentration of dye solutions were monitors using UV-vis spectra at the maximum absorbance of each dye (664nm, 464nm, 554nm, 581nm for MB, MO, RhB and methyl violet, respectively). The results are shown in Figure 6 in text.

Similarly, crystalline solid (100 mg) of **1** was added into 100 mL a binary mixture of MB/MO or MB/RhB at room temperature under stirring. The staring concentration of each dye component in the binary mixture is 10 mg L^{-1}. At given time intervals, the change of the concentration of each dye component was monitored using UV-vis spectra. The results are shown in Figure 7 in text.

Photodegradation experiments of MO or MB.

Crystals (80 mg) of **1** was dispensed into a solution (20.0 mg L^{-1}, 100 mL) MO or MB under stirring. After adding 2.0 mL hydrogen peroxide (30%), the reaction mixture was irradiated with 300W Xe lamp as the visible light source. At given time intervals, the concentration of dyes was measured with UV-vis spectra at the maximum absorbance of the MO or MB dye. Here 2.0 ml peroxide is enough for degradation of dyes and the finally solid obtained by filtration after reaction is green, as the origin color of the as-synthesized crystals of **1**. In comparison, blank experiments were also carried out without catalyst **1** but in the presence of peroxide (2.0 mL). The results are shown in Figure 4a-c in text.

Owing to that complex **1** significantly absorbs MB, different volumes of peroxide were used to evaluate such effects on the degradation of MB. Crystalline solid (80 mg) of **1** was added into 100 mL 20mg L^{-1} MB solution under stirring, and then different amounts (i. e. 0, 1.0, 1.5 and 2.0 mL) of peroxide was added to the solution under visible light irradiation, respectively. At given time intervals, the concentrations of MB were measured by UV-vis spectrometer. After three hours irradiation, the concentrations of MB were almost closed to zero expect the experiment in the absence peroxide. However, when the amount peroxide used is less than 2.0 mL, the finally solid obtained by filtration was blue. The results are shown in Figure 4d in text.

Release and photodegradation experiments of absorbed MB on 1.

20 mg crystalline solid of **1** was dispersed into 300 mL 100 mg L^{-1} MB at room temperature under stirring. After several days, the concentration of MB was not changed and the absorbance was 2.5. The loading of MB was calculated to be 1168 mg g^{-1}. The deep blue solid recycled by filtration was added into 300 mL water under stirring, and at given time intervals, the concentration of the resulting MB solution was measured by UV-vis spectrometer. The results were shown in Figure 8a in text.

Similar photodegradation experiments of absorbed MB were carried out in the presence of different amounts of peroxide. Crystalline solid of **1** (80mg) was added to 100 mL 20mg L^{-1} MB solution under stirring. After 24 hours, the concentration of MB solution was approaching zero, indicating MB are already absorbed completely on **1**, and the solid became blue. The blue solid obtained by filtration was immersed into deionized water, and after adding different amounts of peroxide (2-10mL) under stirring, the reaction mixture was irradiated with 300W Xe lamp as the visible light source. At given time intervals, the concentration of MB solution was measured by UV-vis spectrometer. The results are shown in Figure 8b.

References:

1 W. J. Chang, Y. C. Jiang, S. L. Wang and K. H. Li, *Inorg.Chem.*, 2006, **45**, 6586.
2 X. Xiao, W. W. Ju, W. T. Hou, D. R. Zhu and Y. Xu, *CrystEngComm.*, 2014, **16**, 82.

Table S1. Selected bonds (Å) and angles(°) for **1**

1

Bonds	Dis. (Å)	Bonds	Dis. (Å)	Bonds	Dis. (Å)
Mo(1)-O(6)	1.687(9)	Mo(2)-O(15)	2.062(9)	Mo(4)-O(12)	1.965(10)
Mo(1)-O(7)	1.746(9)	Mo(3)-O(4)	1.689(11)	Mo(4)-Mo(2)#2	3.203(2)
Mo(1)-O(8)#1	1.931(9)	Mo(3)-O(3)	1.727(9)	Cu(1)-N(4)#3	1.981(8)
Mo(1)-O(8)	2.148(9)	Mo(3)-O(5)	1.925(9)	Cu(1)-N(1)	1.985(11)
Mo(2)-O(11)	1.681(11)	Mo(3)-O(8)	2.128(8)	Cu(1)-O(2)	2.147(10)
Mo(2)-O(10)	1.743(9)	Mo(4)-O(13)	1.707(11)	Cu(1)-O(3)	2.161(9)
Mo(2)-O(9)	1.860(10)	Mo(4)-O(14)	1.730(11)	Cu(1)-O(10)#4	2.197(9)
Mo(2)-O(12)	2.046(9)	Mo(4)-O(15)#2	1.879(9)	N(4)-Cu(1)#3	1.981(8)

Bond angles	(°)	Bond angles	(°)
O(6)-Mo(1)-O(7)	104.4(4)	O(4)-Mo(3)-O(8)	102.6(4)
O(6)-Mo(1)-O(5)	102.5(4)	O(13)-Mo(4)-O(12)	103.0(4)
O(7)-Mo(1)-O(5)	99.1(4)	O(14)-Mo(4)-O(12)	99.2(5)
O(11)-Mo(2)-O(10)	105.5(5)	N(4)#3-Cu(1)-N(1)	171.9(4)
O(11)-Mo(2)-O(15)	106.6(5)	N(4)#3-Cu(1)-O(2)	92.3(4)
O(9)-Mo(2)-O(15)	84.4(4)	N(1)-Cu(1)-O(2)	92.8(4)
O(4)-Mo(3)-O(3)	104.4(5)	N(1)-Cu(1)-O(3)	87.3(4)
O(4)-Mo(3)-O(9)	100.7(5)	O(7)#3-Cu(1)-O(3)	105.3(3)

Symmetry codes: #1 -x, -y+1, -z+1 #2 -x, -y+1, -z #3 -x, -y+2, -z+1 #4 x, y+1, z

2

Bonds	Dis. (Å)	Bonds	Dis. (Å)	Bonds	Dis. (Å)
Mo(1)-O(6)	1.707(4)	Mo(2)-O(4)#2	1.927(4)	Cu(1)-O(7)	1.984(4)
Mo(1)-O(5)	1.734(4)	Mo(2)-O(9)	2.114(3)	Cu(1)-N(1)	2.008(4)
Mo(1)-O(7)#1	1.776(4)	Mo(3)-O(10)	1.688(4)	Cu(1)-N(4)#3	2.010(4)
Mo(1)-O(4)	1.856(4)	Mo(3)-O(11)	1.724(4)	Cu(1)-O(5)	2.326(4)
Mo(2)-O(3)	1.679(4)	Mo(3)-O(8)#3	1.920(4)	Cu(1)-O(11)	2.415(4)
Mo(2)-O(2)	1.747(4)	Mo(3)-O(9)#4	1.941(3)	O(9)-Mo(3)#5	1.941(3)
Mo(2)-O(8)	1.907(4)	Cu(1)-O(2)	1.981(4)	N(4)-Cu(1)#3	2.010(4)

Bond angles	(°)	Bond angles	(°)
O(6)-Mo(1)-O(5)	107.4(2)	O(8)#3-Mo(3)-O(9)#4	142.86(15)
O(6)-Mo(1)-O(7)#1	110.04(19)	O(2)-Cu(1)-O(7)	175.49(17)
O(5)-Mo(1)-O(4)	109.05(19)	O(2)-Cu(1)-N(1)	86.64(17)
O(3)-Mo(2)-O(2)	103.92(19)	O(7)-Cu(1)-N(1)	94.58(17)
O(2)-Mo(2)-O(8)	94.88(17)	N(1)-Cu(1)-N(4)#3	170.11(18)
O(2)-Mo(2)-O(9)	154.22(16)	O(7)-Cu(1)-O(5)	89.85(15)
O(10)-Mo(3)-O(11)	104.3(2)	O(7)-Cu(1)-O(11)	80.55(15)
O(10)-Mo(3)-O(8)#3	102.25(18)	N(1)-Cu(1)-O(11)	87.01(15)

Symmetric codes: #1 -x+1, -y+1, -z+1; #2 -x+1, -y+2, -z+1;#3 -x+1, -y+1, -z; #4 x, y-1, z #5

x, y+1, z

Additional Figures

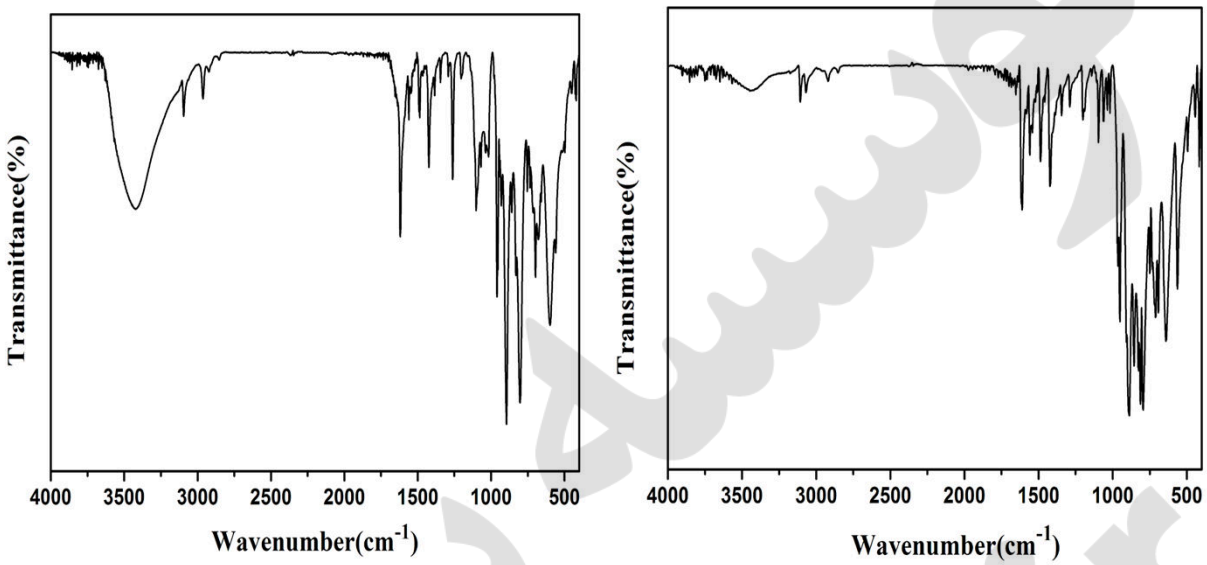

Figure S1. The IR Spectra of complexes **1** (left) and **2** (right).

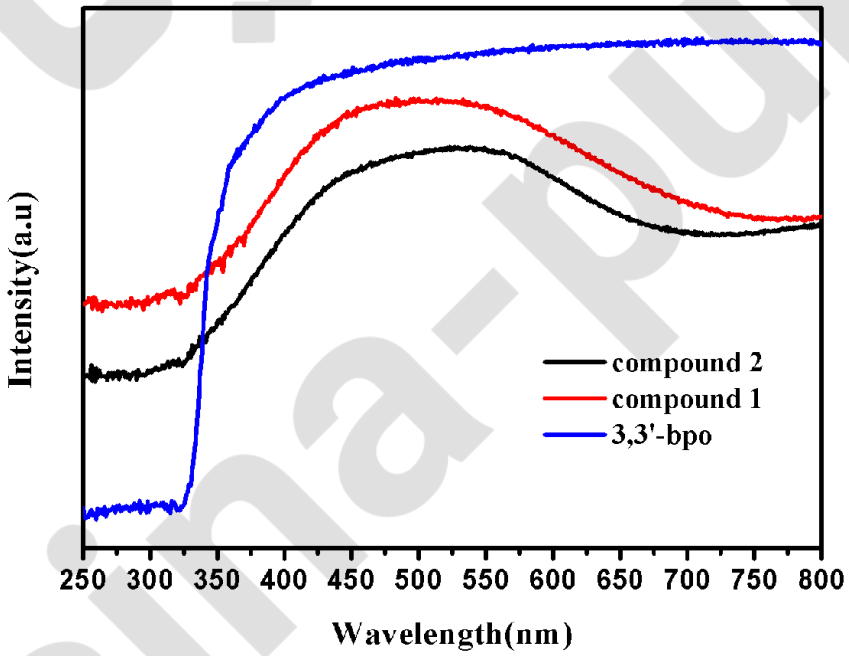

Figure S2. Solid-state emission spectra of the 3, 3'-bpo ligand and complexes **1** and **2** at room temperature.

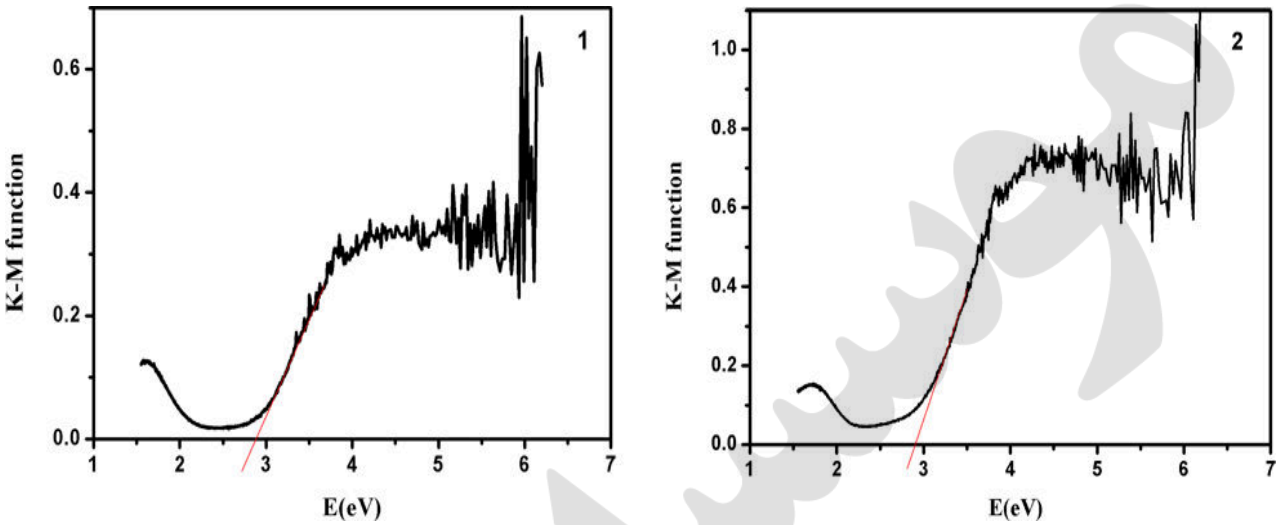

Figure S3. Diffuse reflectance UV-VIS-NIR spectra of K-M functions versus energy (eV) of complexes **1** and **2**.

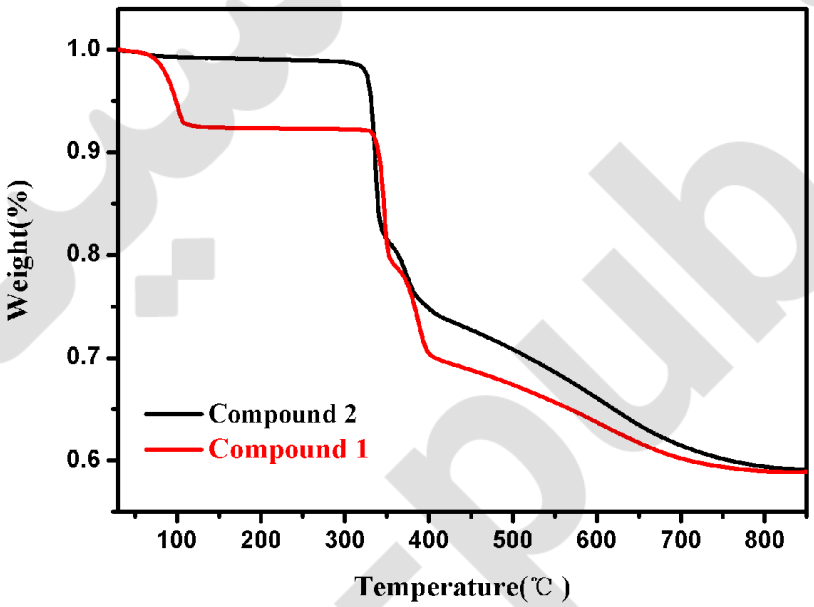

Figure S4. The TGA curves of complexes **1** and **2**.

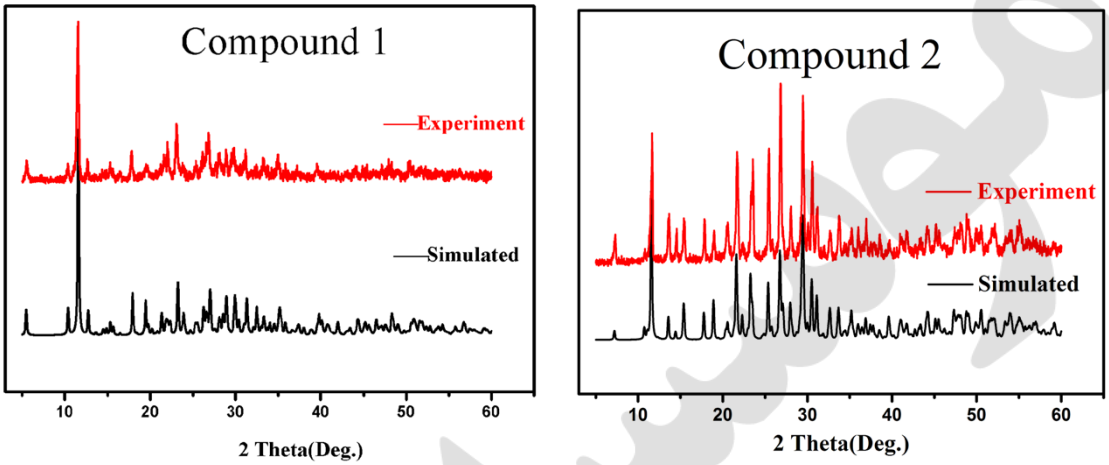

Figure S5. Simulated (black) and experimental (red) PXRD patterns of complexes **1** and **2**.

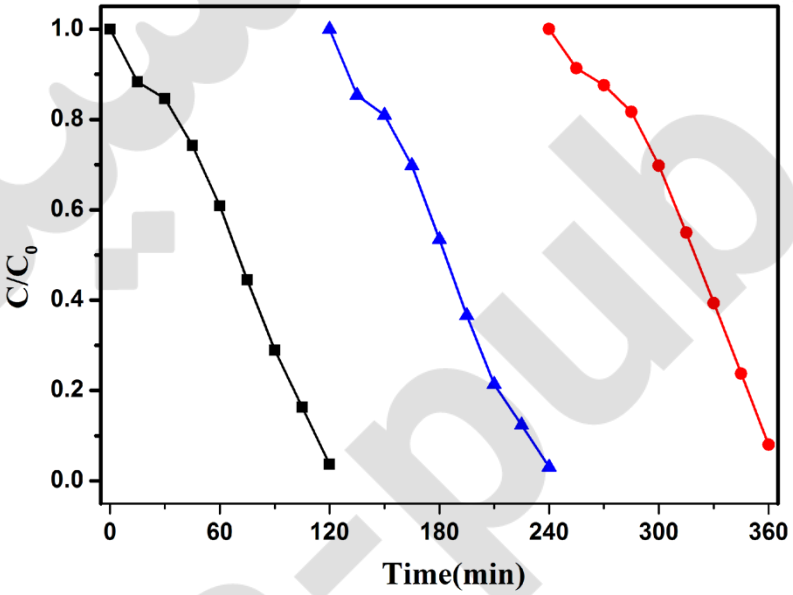

Figure S6. MO photodegradation recyclability test on complex **1** under visible light irradiation.

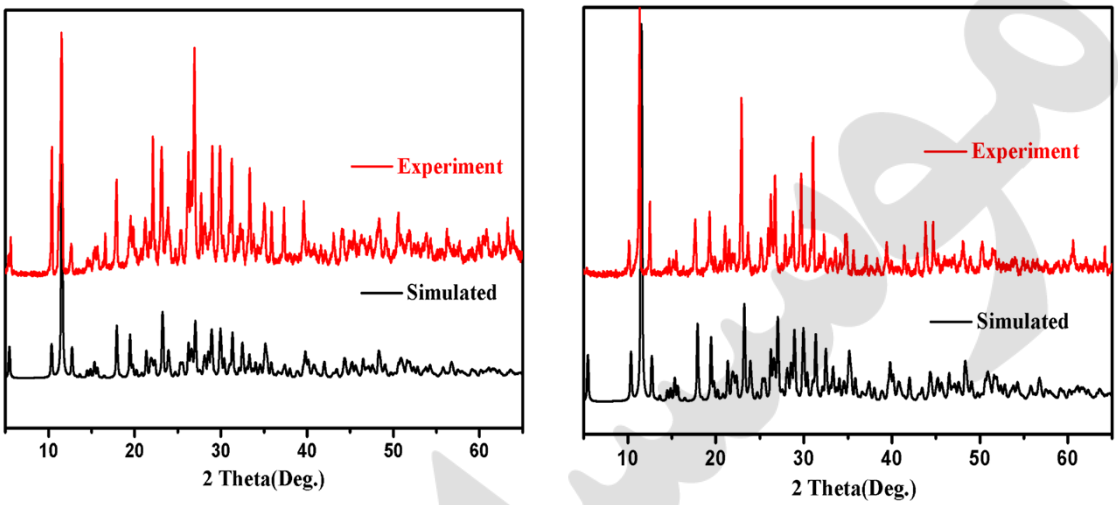

Figure S7. Simulated (black) and experimental (red) PXRD patterns of **1** after MO (left) and MB (right) degradation.

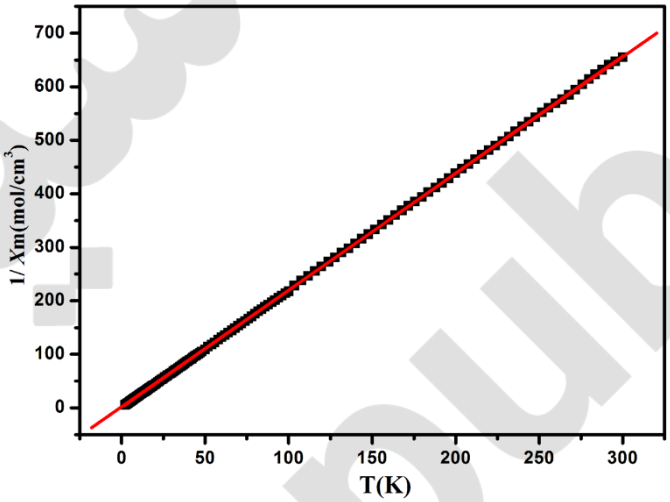

Figure S8. The temperature dependences of χ_m^{-1} for complex **1.**

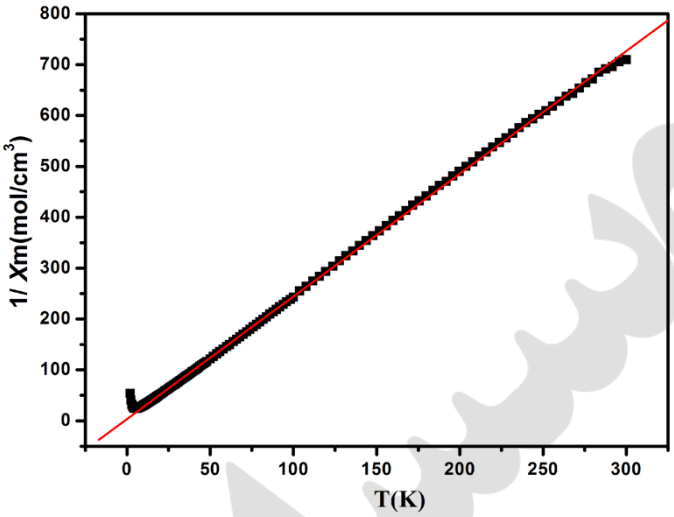

Figure S9. The temperature dependences of χ_m^{-1} for complex **2.**

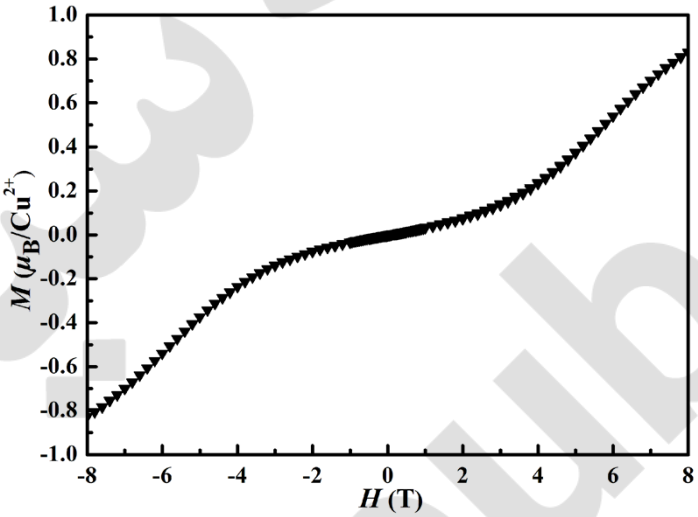

Figure S10. The field dependence (-8 to 8T) of magnetization of **2** at 2K

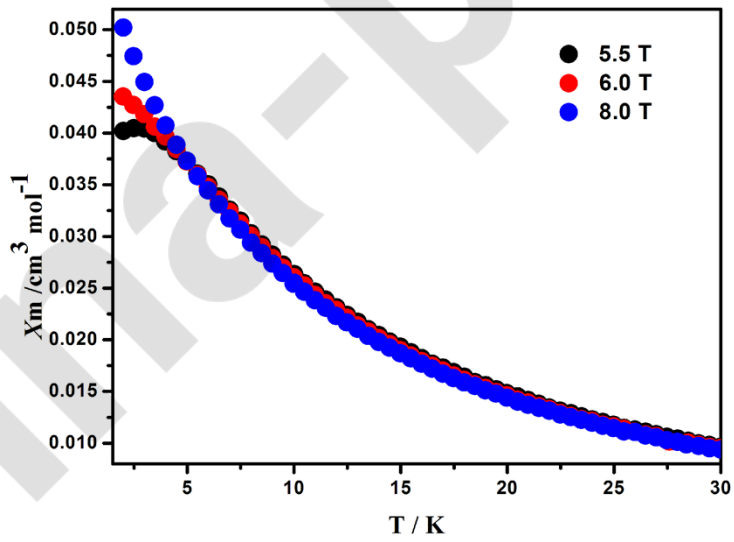

Figure S11. The magnetic susceptibility of **2** at 2-30K in different field